

1 **Reanalysis of the PacIOOS Hawaiian Island Ocean Forecast**  
2 **System, an implementation of the Regional Ocean Modeling**  
3 **System v3.6**

4 **Dale Partridge<sup>1</sup> and Brian S. Powell<sup>1</sup>**

5 <sup>1</sup>University of Hawaii at Manoa, Department of Oceanography, Marine Sciences Building, 1000 Pope Road, Honolulu,

6 Hawaii 96822, USA.

## Abstract

A 10-year reanalysis of the PacIOOS Hawaiian Island Ocean Forecast System was produced using an incremental strong constraint 4D-Variational data assimilation with the Regional Ocean Modeling System (ROMS v3.6). Observations were assimilated from a range of sources: satellite-derived sea surface temperature (SST), salinity (SSS), and height anomalies (SSHA); depth profiles of temperature and salinity from Argo floats, autonomous SeaGliders, shipboard conductivity-temperature-depth (CTDs); and surface HFR velocity measurements from high frequency radar (HFR). The performance of the state-estimate is examined against a free-running forecast showing an improved representation of the observations, especially the realization of HFR surface currents. EOFs of the increments made during the assimilation to the initial conditions and atmospheric forcing components are computed, revealing the variables that are influential in producing the state-estimate solution and the spatial structure the increments form.

## 1 Introduction

The Pacific Integrated Ocean Observing System [*PacIOOS*, 2018] has produced daily forecasts of the ocean state surrounding the Hawaiian Islands since 2009. To facilitate the forecasts a data assimilation procedure is used to incorporate recent observational data into the model to produce the optimal initial state from which to forecast. A number of modeling studies have been performed with older versions of this model to examine various features of the modeling framework, such as the state estimation [*Matthews et al.*, 2012], nested models [*Janeković et al.*, 2013] and the vorticity budget [*Souza et al.*, 2015]. In this work, we perform an extended reanalysis from 2007 to 2017 to coincide with the upgrade of the forecast system to a newer model version and improved processing, in order to produce a consistent data set for further study of the dynamics around Hawai'i.

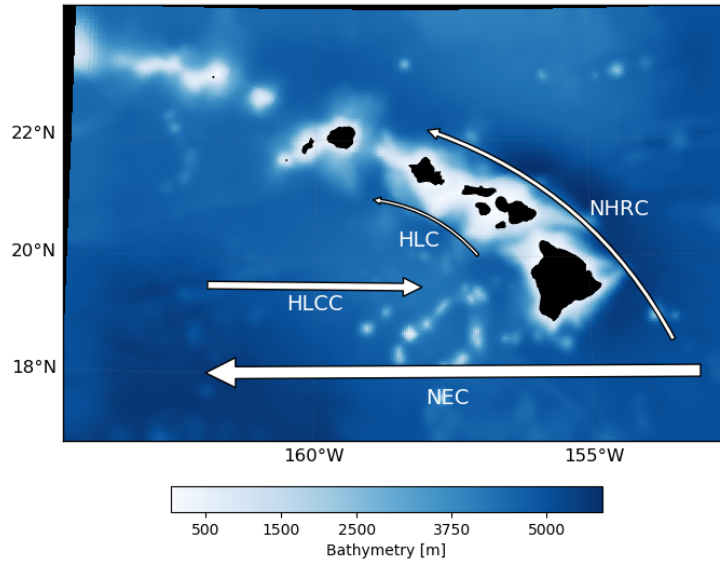
The PacIOOS forecast system uses the time-dependent Incremental Strong constraint 4-dimensional Variational Data Assimilation (I4D-Var) scheme [*Courtier et al.*, 1994; *Moore et al.*, 2004] within the Regional Ocean Modeling System (ROMS) [*Moore et al.*, 2011a; *Powell et al.*, 2008; *Matthews et al.*, 2012] to best reduce the residuals between the model and observations, while maintaining a physically consistent solution. The class of methods known as 4D-Var are state-estimation techniques that create a quadratic cost function to be minimized over a defined time window, utilizing observations at the time they occur in a physically consistent manner to adjust the initial state, boundary conditions, and atmospheric forcing to represent the measurements. The I4D-Var scheme is used in operational centers around the world and solves

39 for increments to the model state, boundary conditions, and atmospheric forcing using the model  
40 physics as a constraint. The combination of I4D-Var within ROMS has been used in previ-  
41 ous studies of various regions [Powell *et al.*, 2008; Broquet *et al.*, 2009; Zhang *et al.*, 2010; Matthews  
42 *et al.*, 2012; Souza *et al.*, 2015]. The details of the model and the observations used within this  
43 study are provided in Section 2.

44 Our model domain covers the Hawaiian Island Archipelago (Figure 1), a dynamically  
45 active region for both the ocean and atmosphere. The North Equatorial Current (NEC), flow-  
46 ing from the east, splits upon encountering the island of Hawai’i, with the bulk transport trav-  
47 eling around the south of the island and continuing west, while the North Hawaiian Ridge Cur-  
48 rent (NHRC) follows the ridge of the other islands in the chain to the north. In the atmosphere,  
49 there are persistent trade winds from the northeast that, combined with steep mountainous ter-  
50 rain on the islands, cause wind wakes in lee of the peaks, particularly on the islands of Hawai’i  
51 and Maui. This introduces strong temperature gradients, increases the seasonal variability [Sasaki  
52 *and Klein*, 2012], and drives smaller currents such as the Hawaiian Lee Countercurrent (HLCC)  
53 [Smith *and Grubišić*, 1993; Xie *et al.*, 2001; Chavanne *et al.*, 2002].

54 There are two main objectives to this study: to assess the skill and performance of the  
55 state-estimation model, and to analyze the increments made to the initial, boundary and atmo-  
56 spheric forcing terms. For the first objective, we compare the state-estimate solution with a  
57 free-running forecast over the decadal time period and examine how the performance changes  
58 over time, utilizing observations derived from satellites and *it situ* measurements. In addition,  
59 PacIOOS operates seven high-frequency radar stations sites across the Hawaiian Islands. The  
60 first station was constructed in 2010, with the remaining six becoming operational over the  
61 period from 2011-2015. These instruments produce high resolution (both spatially and tem-  
62 porally) surface current velocities in the vicinity of the islands of O’ahu and Hawai’i. The use  
63 of HFR observations within a state-estimation scheme has been shown to produce a signifi-  
64 cantly improved representation of surface currents [Souza *et al.*, 2015; Kerry *et al.*, 2016]. The  
65 impact of the radar stations will be a key focus point. The performance assessment is achieved  
66 through the statistics produced by the state-estimation in Section 3, followed by a compari-  
67 son with observations in Section 4. The forecast skill, a measure of the accuracy for a fore-  
68 cast system is computed with reference to a persistence assumption.

69 Section 6 focuses on the second objective of the paper, to examine the increments to the  
70 initial state and atmospheric forcing to determine how the model is adjusted. By evaluating  
71 the Empirical Orthogonal Functions (EOFs) of these increments we determine the spatial pat-



90 **Figure 1.** Model domain and bathymetry, with mean currents labelled from *Lumpkin and Flament* [2013].

72 terns in the variability. Since physical modes are not always independent [*Simmons et al.*, 1983],  
 73 the interpretation of EOF modes must be undertaken with some caution. As such the result-  
 74 ing modes will not necessarily represent a physical phenomenon, but will highlight the vari-  
 75 able spatial patterns made over time by the I4D-Var algorithm.

## 76 **2 Numerical Model and Data Assimilation System**

### 77 **2.1 Model Configuration**

78 The Regional Ocean Modeling System (ROMS) version 3.6 is used to simulate the phys-  
 79 ical ocean around the Hawaiian Islands. ROMS is a free surface, hydrostatic, primitive equa-  
 80 tion model using a stretched coordinate system in the vertical to follow the underwater ter-  
 81 rain. In order to allow varying time steps for the barotropic and baroclinic components, ROMS  
 82 utilizes a split-explicit time stepping scheme (for more details on ROMS, see *Shchepetkin and*  
 83 *McWilliams* [1998, 2003, 2005]).

84 The Hawaiian Island domain covers 164°W to 153°W longitude and 17°N to 23°N lat-  
 85 itude, with bathymetry provided by the Hawaiian Mapping Research Group [*HMRG*, 2017],  
 86 shown in Figure 1. The grid has 4km horizontal resolution with 32 vertical s-levels, config-  
 87 ured to provide a higher resolution in the more variable upper regions. The configuration model,

88 including the method for assimilating surface HFRs and the associated vertical stretching scheme,  
89 is identical to the one first presented in *Souza et al.* [2015].

91 Tidal forcing is produced using the OSU Tidal Prediction Software (OTPS) [*Egbert et al.*,  
92 1994], which is based on the Laplace tidal equations from TOPEX/Poseidon Global Inverse  
93 Solution (TPXO). Tidal constituents included in this simulation are the eight main harmon-  
94 ics;  $M_2$ ,  $S_2$ ,  $N_2$ ,  $K_2$ ,  $K_1$ ,  $O_1$ ,  $P_1$ ,  $Q_1$ , as well as two long period and one non-linear constituent;  
95  $M_f$ ,  $M_m$  and  $M_4$ . To avoid any long term drifting of the tidal phases related to constituents we  
96 do not consider, the tidal harmonics are updated each year to define the phases in terms of the  
97 start of that year.

98 Lateral boundary conditions are taken from the HYbrid Coordinate Ocean Model (HY-  
99 COM) [*Chassignet et al.*, 2007] and are applied daily. Within ROMs, we apply the boundary  
100 differently for each variable; Chapman [*Chapman*, 1985] conditions are applied to the free sur-  
101 face, Flather [*Flather*, 1976] conditions for transferring momentum from 2D barotropic en-  
102 ergy out of the domain, while the 3D momentum and tracers variables are clamped to match  
103 HYCOM. A sponge layer of 12 grid cells (48km) linearly relaxes the viscosity by a factor of  
104 four and diffusivity by a factor of two close to the boundary to account for imbalances between  
105 HYCOM and ROMS.

106 From 2007-2009, atmospheric forcing is provided by coarse  $2^\circ$  resolution NCEP reanal-  
107 ysis fields. The wind fields are statistically combined with a fine-scale PSU/NCAR mesoscale  
108 model (MM5) [*Yang et al.*, 2008a]. From July 2009, atmospheric forcing is provided locally  
109 by a high-resolution Weather Regional Forecast (WRF) model [*WRF-ARW*, 2017]. WRF sup-  
110 plies information about surface air pressure, surface air temperature, long- and short-wave ra-  
111 diation, relative humidity, rain fall rate, and 10m wind speeds. The ocean model is forced us-  
112 ing this data every six hours, taken from the atmospheric model with 6km resolution across  
113 the entire domain.

114 Prior to the experiment, a six-year non-assimilative model was run using the same ini-  
115 tial state, boundary conditions, and atmospheric forcing. The variability of the model is used  
116 to produce an estimate of the background error covariances used within I4D-Var, as well as  
117 the mean sea surface height to use with sea level anomaly observations.

118 A detailed derivation of the I4D-Var cost function can be found in [*Kerry et al.*, 2016;  
119 *Penenko*, 2009; *Weaver et al.*, 2003; *Stammer et al.*, 2002; *Talagrand and Courtier*, 1987]. To  
120 formulate the solution, we must provide estimates of the uncertainty in both the model and  
121 observations. The model uncertainty,  $\mathbf{P}$ , is estimated using the variability of the six-year run

122 described above, while observation uncertainty,  $\mathbf{R}$ , is assumed to be diagonal, (i.e. observa-  
123 tions are independent). The implementation of I4D-Var in ROMS is covered extensively in [Moore  
124 *et al.*, 2011a,b,c].

## 125 **2.2 Experiment Setup**

126 The reanalysis covers a period of 10 years, from July 2007 to July 2017. The minimiza-  
127 tion of the cost function first updates the nonlinear model in an *outer* loop, before perform-  
128 ing a linear least-squares procedure over multiple *inner* loops. For this grid there is a suffi-  
129 cient reduction in  $J$  using a single outer loop with 13 inner loops to efficiently run the sim-  
130 ulation at an acceptable computational cost. The period of assimilation for the IS4D-Var cy-  
131 cles is four days, which corresponds to the limit of the linearity assumption within the domain  
132 [Matthews *et al.*, 2011]. The atmospheric forcing is adjusted every six hours, while the bound-  
133 aries are every 12h. An analysis of these adjustments is performed in Section 6.

134 Eight day forecasts are performed from the end of each cycle using the assimilated state  
135 as initial conditions, and the short-range (1-4 days) and mid-range (5-8 days) forecasts are eval-  
136 uated for skill.

## 137 **2.3 Observations**

138 Observational data used within this study include satellite measurements of the ocean  
139 surface of temperature, height, and salinity, *in situ* depth profiles of temperature and salinity,  
140 and surface HFR velocities from High Frequency Radar. Observations close to the boundary  
141 and in shallow water are neglected.

### 142 **2.3.1 Satellite Derived Measurements**

143 Sea Surface Temperature (SST) observations are available from two sources at differ-  
144 ent time periods: initially we used the Global Ocean Data Assimilation Experiment High Res-  
145 olution Sea Surface Temperature (GHRSSST) Level 4 OSTIA Global Foundation Sea Surface  
146 Temperature Analysis [PO.DAAC, 2005], referred to as OSTIA for this work. The data is dis-  
147 tributed by the Physical Oceanography Distributed Active Archive Center (PO.DAAC), using  
148 optimal interpolation to combine data from the Advanced Very High Resolution Radiometer  
149 (AVHRR), the Advanced Along Track Scanning Radiometer (AATSR), the Spinning Enhanced  
150 Visible and Infrared Imager (SEVIRI), the Advanced Microwave Scanning Radiometer-EOS

151 (AMSRE), the Tropical Rainfall Measuring Mission Microwave Imager (TMI), and *in situ* data.  
152 This distribution provides a highly smoothed daily gridded global dataset at the surface at a  
153 6km spatial resolution, accurate between 0.2 – 0.5 °C in the domain.

154 Beginning in April 2008, we switched to using the GHRSSST Level 4 K10\_SST Global  
155 1 meter Sea Surface Temperature Analysis data set [*PO.DAAC*, 2008], produced by the Naval  
156 Oceanographic Office, and is referred to as NAVO for this work. Also distributed by *PO.DAAC*,  
157 this product combines, in a weighted average, data from AVHRR, AMSRE and the Geosta-  
158 tionary Operational Environmental Satellite (GOES) Imager. This distribution provides a daily  
159 gridded global dataset at 1 meter depth at a 10km spatial resolution, accurate to 0.4 °C in the  
160 domain.

161 Sea Surface Height (SSH) observations are derived using sea level anomaly data from  
162 the Archiving, Validation and Interpretation of Satellite Oceanographic data (AVISO) delayed  
163 time along track information. The data comes from multiple altimeter satellites measuring the  
164 anomaly with respect to a twenty-year mean SSH, homogenized against one of the missions  
165 to ensure consistency. Each track has approximately 7km spatial resolution and will usually  
166 make multiple passes through our domain each day. To convert from sea level anomaly to sea  
167 surface height we add the mean SSH field taken from the six-year model run described early,  
168 to which we add the barotropic tidal prediction from TPXO. The accuracy of the swaths de-  
169 pend on the source satellite and range from 5–7cm. We use the AVISO product that has been  
170 fully filtered and quality controlled until May 2016. At the time of the experiment, the delayed  
171 time data were unavailable beyond May 2016, so the near real-time data were used.

172 Sea Surface Salinity (SSS) data are taken from Aquarius missions daily L3 gridded data  
173 set [*PO.DAAC*, 2015] distributed by *PO.DAAC*. The satellite uses a combination of radiome-  
174 ters and scatterometers to estimate the surface salinity, mapped to a coarse 1° resolution. Er-  
175 rors for this product are around 0.2 ppt. Data for this product are available from August 2011  
176 until June 2015.

### 177 **2.3.2 In Situ Measurements**

178 Depth profiles of temperature and salinity are obtained from three sources: the Hawaii  
179 Ocean Time-Series (HOT) shipboard Conductivity Temperature Depth (CTD) casts, the global  
180 network of Argo floats, and autonomous SeaGliders operated by the University of Hawaii.

181 The Hawaii Ocean Time-Series (HOT) project conducts monthly cruises to the deep wa-  
182 ter A Long-term Oligotrophic Habitat Assessment (ALOHA) station (located at 23° 45'N, 158°

183 00°W) in order to develop a long term data set of physical and biochemical ocean informa-  
184 tion CTD stations of temperature and salinity are concentrated in the region around the sta-  
185 tion; although some are also established along the ship route.

186 HOT also conducts regular SeaGlider missions departing from station ALOHA. In ad-  
187 dition, PacIOOS conducts occasional SeaGlider surveys in areas close to the south coast of  
188 Oahu. The buoyancy driven autonomous underwater vehicles take profiles and transects at depth  
189 of temperature and salinity.

190 Observations from the global Argo float network are available from the Argo array Net-  
191 work [USGODAE, 2016]. The free-drifting floats profile temperature and salinity during as-  
192 cension and descension every 10 days of depths down to 2000m [Oka and Ando, 2004]. Argo  
193 measurements tend to occur in the model domain at a rate of about 1-2 profiles per day.

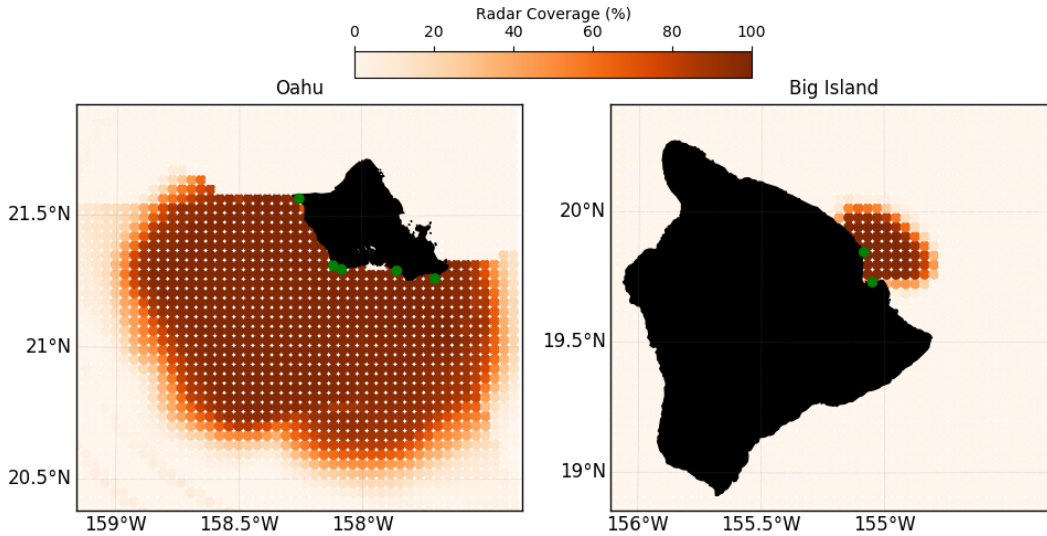
194 Representational errors for HOT CTDs, Argo Floats, and SeaGliders are defined by the  
195 variance of observational data from all available sources across the Pacific sorted into depth  
196 bins. These profiles resemble a typical temperature/salinity profile, with a peak temperature  
197 error of 0.8K, and peak salinity error of 0.15ppt occurring in the mix layer at a depth around  
198 100m.

### 199 ***2.3.3 High Frequency Radar Measurements***

200 HFR measurements of surface currents are available from PacIOOS at seven sites around  
201 the Hawaiian islands: five around the south-west of Oahu and two on the east coast of the Big  
202 Island. Data is available from the first site in October, 2010 with the other sites coming on-  
203 line at various times, the most recent being October, 2015. The range for the HFRs on Oahu  
204 extend approximately 150km from the coast, while the two Big Island sites are focused on cur-  
205 rents around Hilo bay and have a shorter range. At the range limits, HFR data is less reliable.  
206 Figure 2 shows the percentage availability of data in the region. Data is counted as available  
207 if there is more than 80% in a given week.

208 Both spatially and temporally, the resolution for all sites is significantly higher than the  
209 model resolution. The HFR data are low-pass filtered at 3 hours to remove the high frequency  
210 signals that may not be resolved by the model (atmospheric forcing fields are every 3 hours).  
211 We then provide the spatial field of data every 3 hours. The associated error is calculated in-  
212 dividually for each spatial point as the accuracy of the measurements is determined by the lev-  
213 els of interference, which increases with range. For each observation point we calculate the





216 **Figure 2.** Composite image of percentage coverage for all radar sites (situated at green dots) when all are  
 217 operational. Where two sites overlap the greater value is taken to indicate the level of coverage at each point.

214 power spectral density and calculate the noise as per *Zanife et al.* [2003], with a minimum of  
 215 7cm/s. At the extreme, errors may reach 17cm/s.

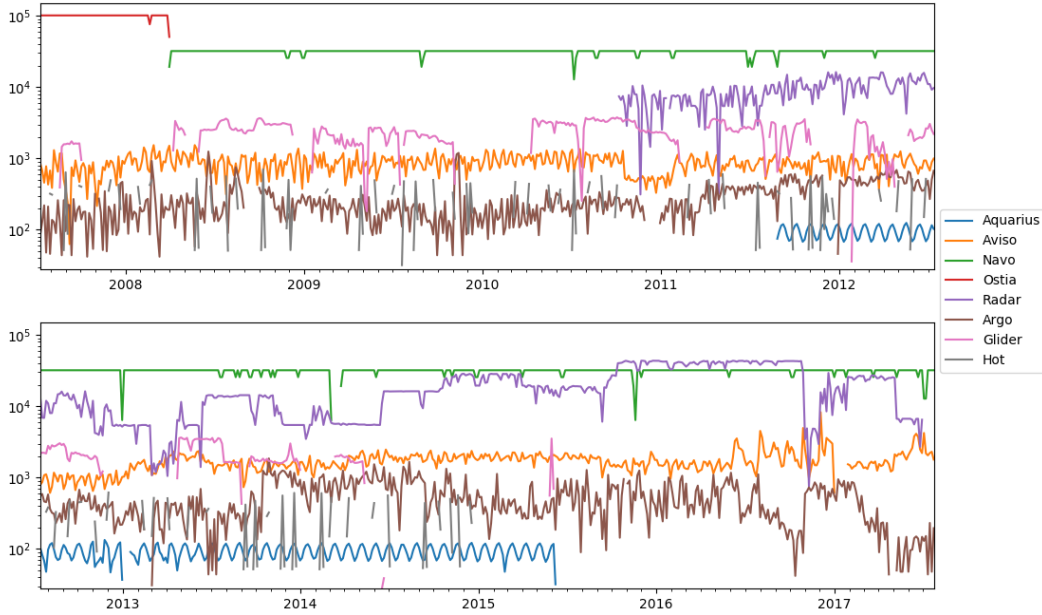
218 The number of observations for each four day cycle from all sources are shown in Fig-  
 219 ure 3. Sea surface temperature measurements from both OSTIA and NAVO are consistently  
 220 the most available observation source, and by the end of the time period HFR is supplying a  
 221 similar quantity. *In situ* measurements, which include both temperature and salinity for each  
 222 of the instruments, provide a smaller amount of data by an order of magnitude.

### 225 3 Assimilation Statistics

226 In this section we examine the state estimate to quantify the performance during our time  
 227 period.

#### 228 3.1 Cost Function Reduction

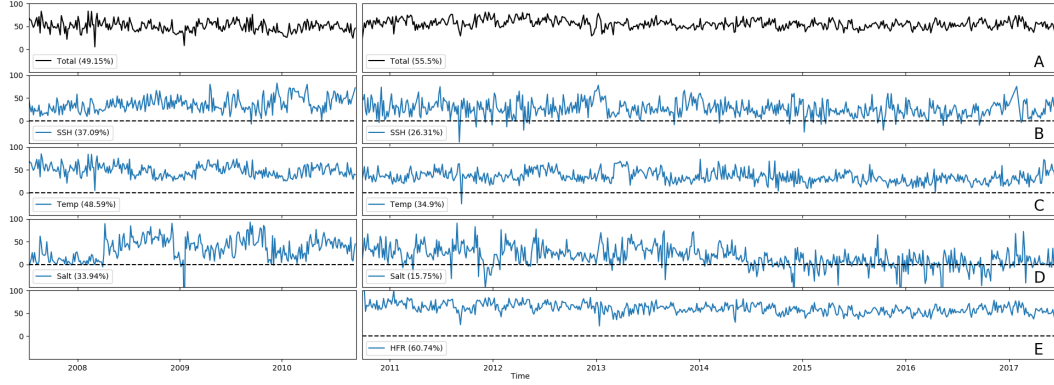
229 I4D-Var minimizes the residuals between the model and observations over each 4-day  
 230 cycle. We calculate the percentage reduction between the initial and final cost function for each  
 231 cycle to assess how the assimilation performs over time. Additionally, we can breakdown the  
 232 cost function further to examine in detail which observation types are reduced the most, how-  
 233 ever it should be noted that this breakdown does not distinguish between observation sources.



223 **Figure 3.** Number of observations used within data assimilation run. Note that there tend to be orders of  
 224 magnitude more satellite or remotely-sensed observations than *in situ*.

234 Figure 4 shows a time series of this percentage reduction in the cost function for each  
 235 of the variables we observe: sea surface height, temperature, salinity and HFR, in addition to  
 236 the total reduction. A value of 0 means the final cost function is the same as the initial and  
 237 no reduction has occurred. The plot is split into two distinct time periods, before and after the  
 238 HFR observations are introduced in order to assess changes in the relative contributions of each  
 239 variable to the overall reduction.

240 The total cost function of all data (Figure 4A) is on average halved for each cycle, with  
 241 an improvement from 49% of the original value to 55% when HFR observations are available.  
 242 Looking at the breakdown in Figure 4B-E we see that the final cost function associated with  
 243 the other observed variables: sea surface height, temperature, and salinity, is reduced by a smaller  
 244 percentage than before HFR was included, which might be expected given the quantity of HFR  
 245 observations. Salt measurements tend to contribute the least improvement (34% pre-HFR, 16%  
 246 post-HFR) as they are the least numerous. In some cases, the percent reduction of the cost func-  
 247 tion for salt is negative, particularly after the Aquarius satellite mission has ended and there  
 248 were fewer *in situ* observations used. The cost function associated with HFR measurements  
 249 is reduced by 60% of the initial value, meaning the model is significantly closer to the HFR  
 250 observations after the assimilation.



251 **Figure 4.** Time-Series of percentage reduction in the I4D-Var cost function; Left column are pre-HFR  
 252 observations, right post-HFR, with the mean value given in parentheses. Dashed lines mark the limit of 0,  
 253 below which there is no reduction in the cost function for that variable. A) Total cost function reduction for all  
 254 observations; B) Sea surface height observations, C) Temperature observations; D) Salinity observations; E)  
 255 HFR observations.

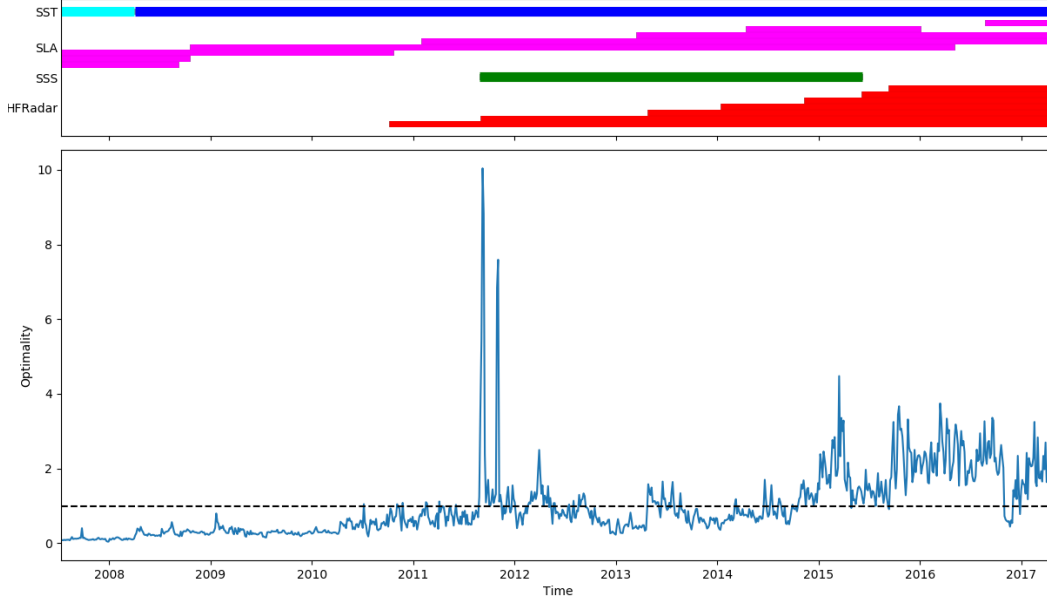
### 256 3.2 Optimality

Another measure of the performance is the theoretical minimum value of the cost function [Bennett, 2002; Powell et al., 2008], which states that:

$$\frac{2J_{min}}{N_{obs}} = 1, \quad (1)$$

257 where  $N_{obs}$  is the number of observations. Assuming the conjugate gradient algorithm con-  
 258 verges, Equation (1) provides a simple representation of how consistently the errors ( $\mathbf{P}$  and  
 259  $\mathbf{R}$ ) are specified, since the error covariances define the cost function. Figure 5 shows a time-  
 260 series of the calculated optimality value for the model run, in addition to a timeline of the avail-  
 261 ability of certain observations for reference. Over the full time period the mean optimality is  
 262 0.95; however there are large differences over the course of the time period. In the pre-HFR  
 263 period the optimality is low, suggesting that the error bounds on observations are too wide.  
 264 Since SST is the dominant source of observations before HFR, the prescribed errors associ-  
 265 ated with SST may be too large.

266 Post-HFR the optimality value increases, suggesting the errors in this period are under-  
 267 estimated. A large optimality value arises when the cost function is large, i.e. large differences  
 268 between the model and observations. There were two anomalous cycles in 2011, the first of  
 269 which coincides with the introduction of a second radar site. From 2012 onwards the optimal-  
 270 ity value is generally good, if highly variable. The trend of increase in optimality given the



273 **Figure 5.** Top - Gantt chart of remotely sensed observations used in the study. Bottom - Optimality of  
 274 4D-Var Assimilation Experiment with the dashed line representing the theoretical minimum.

271 available observations points to an underestimation of HFR errors, or at the least a persistent  
 272 difference between the model and HFR observations.

### 275 3.3 Error Consistency

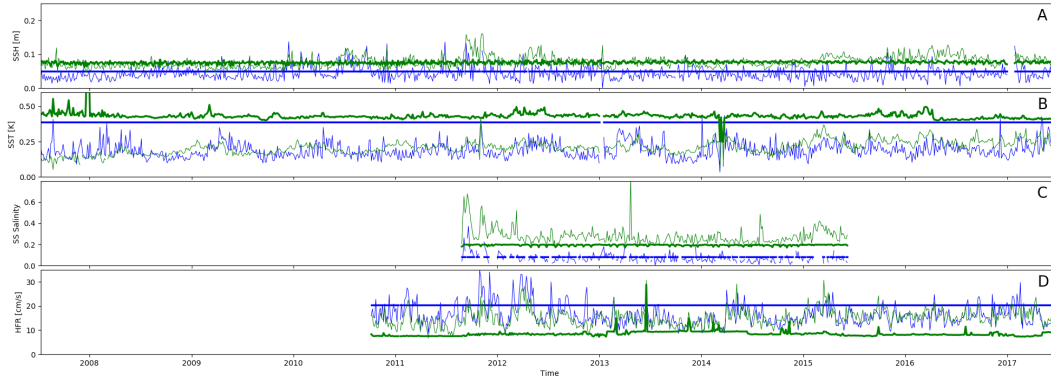
A more detailed examination of the consistency of the errors follows the diagnostics described in [Moore *et al.*, 2011b; Matthews *et al.*, 2012]. If the variances in  $\mathbf{P}$  and  $\mathbf{R}$  are correctly specified *a priori*, they will be consistent with the *a posteriori* estimated via:

$$(\widetilde{\sigma}_i^b)^2 = \frac{1}{p_i} \sum_{j=1}^{p_i} (\mathcal{H}_j(\mathbf{x}^a) - \mathcal{H}_j(\mathbf{x}^b))(y_j - \mathcal{H}_j(\mathbf{x}^b)) \quad \text{and} \quad (2)$$

$$(\widetilde{\sigma}_i^o)^2 = \frac{1}{p_i} \sum_{j=1}^{p_i} (y_j - \mathcal{H}_j(\mathbf{x}^a))(y_j - \mathcal{H}_j(\mathbf{x}^b)), \quad (3)$$

276 where  $i$  refers to the observation type,  $p_i$  is the number of observations of that time,  $y_j$  is the  
 277 value of observation  $j$  of type  $i$ , and  $\mathcal{H}_j$  is the mapping of the model background ( $\mathbf{x}^b$ ) or anal-  
 278 ysis ( $\mathbf{x}^a$ ) to observation  $j$ .

279 Figure 6 shows both the *a priori* and *a posteriori* errors for the remotely sensed data.  
 280 The observation *a priori* values are calculated as the mean error of the observations in each  
 281 cycle, while the background *a priori* values are defined as the variability of a free running non-  
 282 linear model. If the *a posteriori* errors are typically larger than the *a priori*, it implies the ini-



300 **Figure 6.** Time series of spatially averaged background (blue) and observation (green) errors, with thick  
 301 lines showing *a priori* values and thin lines the posterior calculated using Equations (2) and (3). A) Sea  
 302 Surface Height; B) Sea Surface Temperature; C) Sea Surface Salinity and D) HFR.

283 tial errors in **P** and **R** are underestimated. Conversely, if they are smaller the initial errors are  
 284 likely overestimated.

285 Figure 6A shows that sea surface height errors are consistent, while sea surface temper-  
 286 ature, Figure 6B suggests the *a priori* errors are overestimated. The *a priori* observation er-  
 287 rors for NAVO SST observations are defined with a minimum error of 0.4K, but the *a pos-*  
 288 *teriori* are more typically around 0.25K. The *a priori* background errors also appear over-  
 289 estimated.

290 Sea surface salinity observation errors (fig. 6C) are slightly underestimated but gener-  
 291 ally consistent, as are the background errors. The HFR observation errors (fig. 6D) also ap-  
 292 pear to be underestimated, with most *a priori* errors close to the minimum value of 7cm/s. The  
 293 *a posteriori* errors suggest a typical value of around 12 – 15cm/s would be more appropri-  
 294 ate. The *a priori* background errors are reasonably consistent with the *a posteriori*, if anything  
 295 they are slightly overestimated.

296 This error consistency analysis supports the conclusions in Section 3.2 that the SST obser-  
 297 vation errors are overestimated and HFR values are underestimated. It is worth noting that  
 298 these diagnostics are only estimates used to characterize the errors and are not the true pos-  
 299 terior error.

## 4 Comparison with Observations

Because I4D-Var relies on the model physics to represent observations through time, it should provide better forecasts. Other methods that perturb the state at single times may better reduce the time-fixed cost function, but can add non-physical structures that generate noisy forecasts.

In this section we examine the state estimate solution by comparing the model to observations. For reference, the observations are also compared against a free-running forecast starting from the same time as each state-estimate cycle. All boundary, atmospheric and tidal forcings are initially the same between runs; however, the boundary and atmospheric forcing are altered as part of the state estimate solution. For comparing fields we use the Root Mean Squared Anomaly (RMSA) and the Anomaly Correlation Coefficient (ACC), defined as:

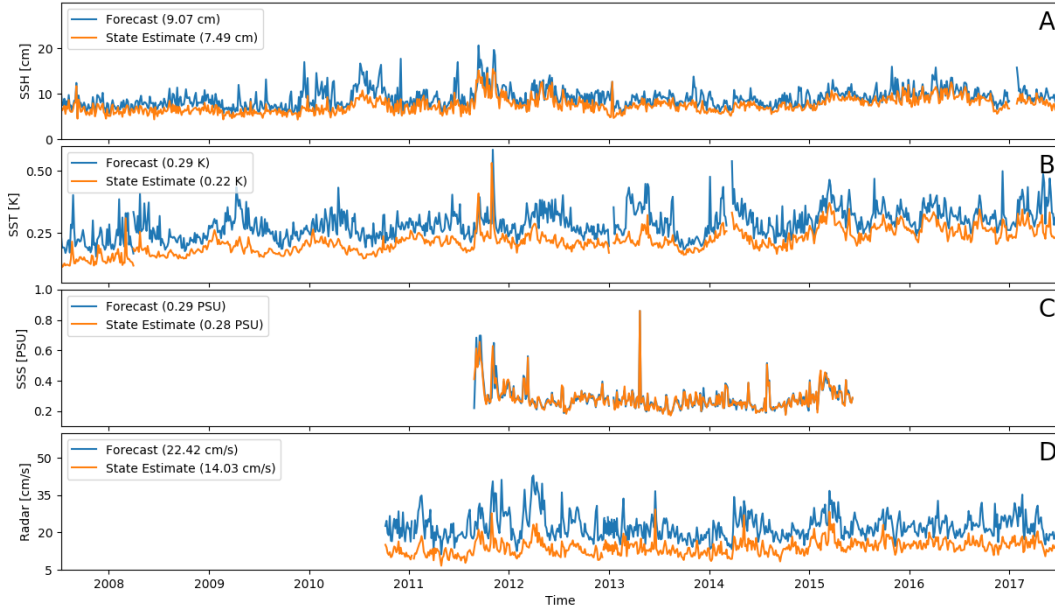
$$\text{RMSA}(\mathbf{x}, \mathbf{y}) = \sqrt{\frac{1}{N} \sum_{i=1}^N ((x_i - \bar{x}) - (y_i - \bar{y}))^2} \quad (4)$$

$$\text{and} \quad \text{ACC}(\mathbf{x}, \mathbf{y}) = \frac{\sum_{i=1}^N (x_i - \bar{x})(y_i - \bar{y})}{\sqrt{\sum_{i=1}^N (x_i - \bar{x})^2 \sum_{i=1}^N (y_i - \bar{y})^2}}, \quad (5)$$

where  $N$  is the number of observations and  $x$  are the model values at the same location and time as the observations  $y$ . The RMSA provides a measure of the residual between the model and observations, while the ACC determines the strength of the relationship between the two. We can calculate values for a single spatial point throughout time, or for all spatial points at a single time; however, we require there must be at least 20 observation values available to get a representative statistic. The gridded satellite products are ideally suited to this analysis, while the depth profiles from *in situ* measurements are binned into 50m depth layers to ensure a minimum number of values.

### 4.1 Remotely Sensed Observations

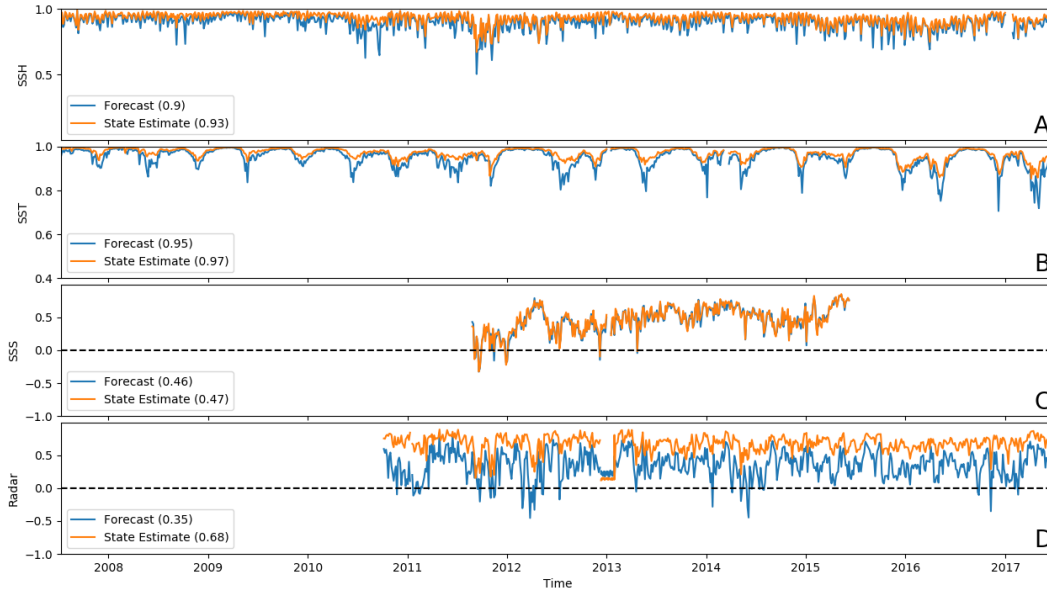
Figure 7 shows the RMSA between the observations and the models for each source of remotely observed data. The state-estimate solution reduces the RMSA compared with the free-running forecast by 1.58cm (17%), 0.07K (24%), 0.01PSU (3%) and 8.39cm/s (37%) for sea surface height, sea surface temperature, sea surface salinity and HFR respectively. In Figure 7A the RMSA of the state-estimate solution is close to the typical observational error of 7cm, while in Figure 7B we see the RMSA is comfortably less than the 0.4K representative error. Sea surface salinity is only marginally improved by the state-estimate solution, but is slightly over the prescribed observational error of 0.2PSU. The RMSA of the currents associated with HFR



328 **Figure 7.** Time series of root mean squared anomalies (RMSA) between remotely sensed observations and  
 329 two model realizations; the state estimate and a free running forecast. A) Sea Surface Height; B) Sea Surface  
 330 Temperature; c) Sea Surface Salinity and D) HFRs

325 observations, shown in Figure 7D, is improved greatly by the state-estimation; however, the  
 326 mean value of 14cm is around double the typical error prescribed *a priori* of 7cm. As shown  
 327 in the previous sections, this error was underestimated.

334 The ACC is also improved by the state-estimate for all variables, as shown in Figure 8.  
 335 For sea surface height, temperature and salinity the improvement is small due to a significant  
 336 agreement in the forecast with gains of 0.03, 0.02, and 0.01 respectively. The improvement  
 337 in HFR is much more significant, with an average correlation improvement from 0.35 to 0.68.  
 338 As shown in Figure 8D the free-running forecast model can diverge from the observations enough  
 339 to become negatively correlated over a cycle, while the state-estimate solution is consistently  
 340 positively correlated. Figure 9 shows the spatial RMSA between the forecast and analyses model  
 341 solutions and the observations for both sources of sea surface temperature observations: OS-  
 342 TIA and NAVO. In both cases there is a clear reduction in the RMSA, with the largest source  
 343 of error in the areas leeward of the islands, most notably the island of Hawai'i. This is due  
 344 to higher heat flux variability from a reduction in cloud cover [Yang *et al.*, 2008b; Matthews  
 345 *et al.*, 2012]. Even in this peak area, the state-estimate solution is around the observational er-  
 346 ror of representativeness of 0.4K, meaning the model is performing well with regards to SST.

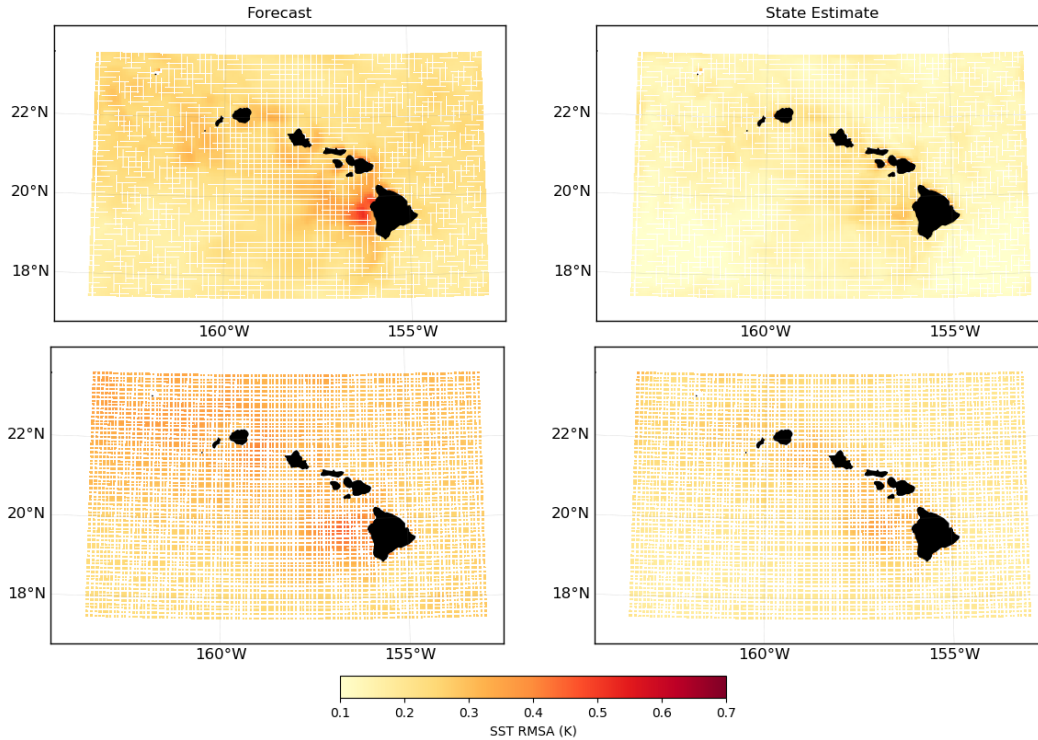


331 **Figure 8.** Time series of anomaly correlation coefficients (ACC) between remotely sensed observations and  
 332 two model realizations; the state estimate and a free running forecast. A) Sea Surface Height; B) Sea Surface  
 333 Temperature; c) Sea Surface Salinity and D) HFRs

349 Both RMSA and ACC between the experiments and HFR observations are shown in Fig-  
 350 ure 10 for the island of O’ahu. The RMSA of the free-running forecast is reasonably uniform  
 351 across the region covered by the HFR, around 20–25cm/s with some varying values around  
 352 the extent of the radar coverage. The inclusion of HFR observations in the state-estimate so-  
 353 lution leads to significantly reduced values of 12 – 15cm/s, a reduction of almost half. The  
 354 ACC is also significantly improved from a weak correlation to a consistently strong positive  
 355 one.

356 As discussed in *Souza et al.* [2015], there are several reasons the model can differ from  
 357 surface current observations: the discretization of the model, imperfect stratification, differ-  
 358 ing barotropic-to-baroclinic tide conversion at Kaena ridge, or mixing parameters that do not  
 359 capture the real baroclinic mixing. This may lead to a different location of the currents in the  
 360 model from those observed by the HFR; however, the model does a good job reducing these  
 361 errors [*Janeković and Powell, 2012*]. The HFRs located on the island of Hawai’i have a smaller  
 362 coverage region, but the level of improvement from the forecast to the state-estimate solution  
 363 is consistent with the O’ahu results shown here.



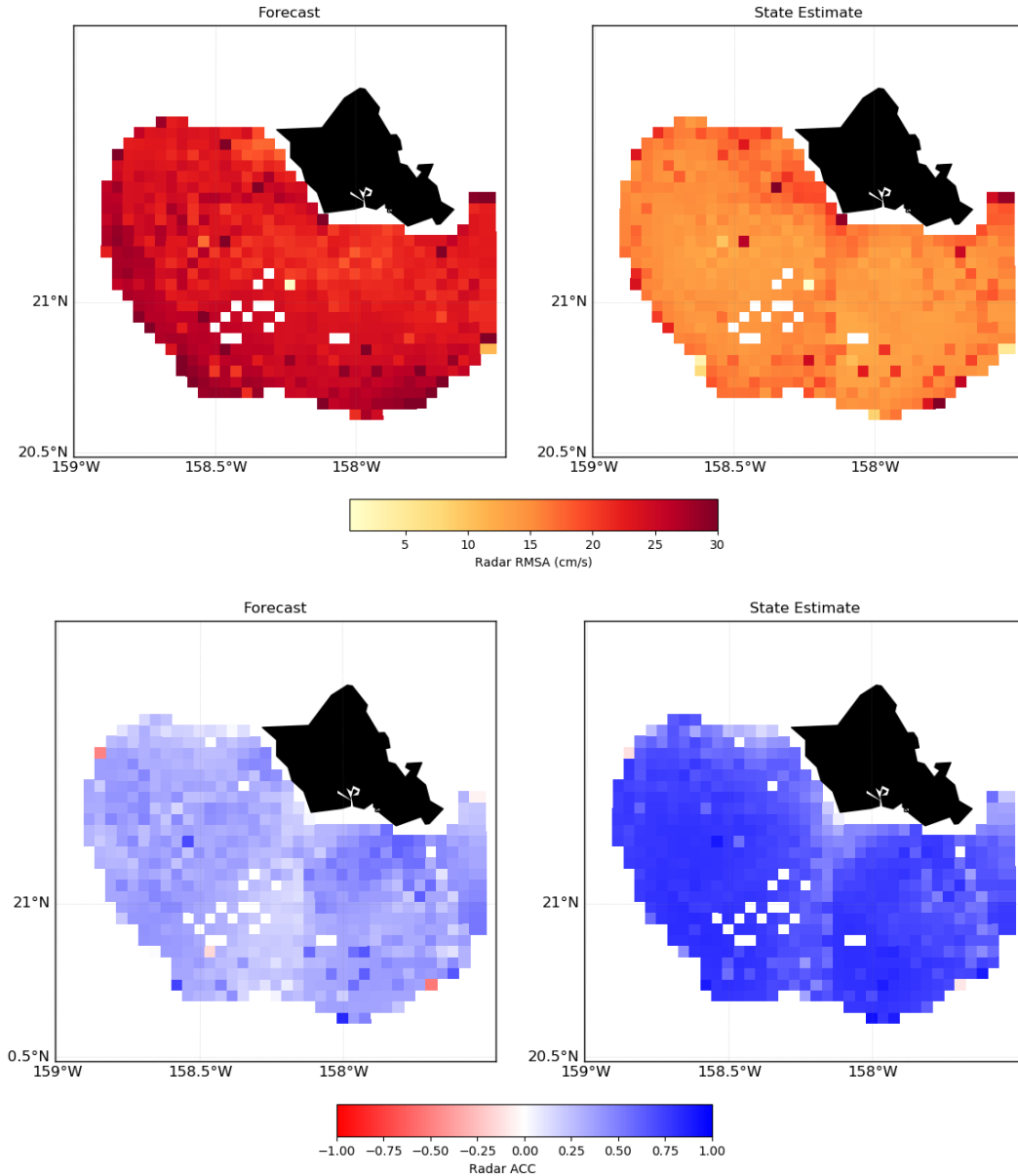


347 **Figure 9.** Spatial maps of RMSA for SST observation sources. Top - OSTIA data (2007-2008); Bottom -  
 348 NAVO data (2008-2017). Typical error of representativeness is around 0.4K.

## 365 4.2 Subsurface Observations

366 The *in situ* observation sources: Argo floats, Seagliders and HOT CTDs also show an  
 367 improvement in the state estimate over the forecast. The subsurface temperature RMSA val-  
 368 ues are reduced by an average of 0.03K (5%) and salinity by 0.01PSU (9%). The average val-  
 369 ues are within the bounds of the maximum representative errors for both variables, 0.8K and  
 370 0.15PSU; however, there are several occasions when the RMSA value for a cycle exceeds that  
 371 limit. In those cases the state-estimate is reducing the cost, but there are too few observations  
 372 to weight the model towards.

373 Figure 11 shows the RMSA and ACC profiles for temperature and salinity respectively  
 374 for each source of subsurface observation. For all three sources, the greatest RMSA between  
 375 the models and observations is along the thermocline where minor differences in thermocline  
 376 depth leads to temperature differences. The state-estimate improves the RMSA in this region  
 377 by 10–15%. The thermocline location is also the source of lowest correlation between the



364

**Figure 10.** Spatial maps of HFR statistics for south O’ahu. Top - RMSA; Bottom - ACC.

378

observations and the model, which is also improved by the state-estimate by  $\sim 5\%$ . There is a high RMSA for SeaGliders at the base of their profiles (close to 1000m), in this instance the state-estimate performs worse than the forecast. Many of the Glider missions used operate in the shallow waters off the south coast of O’ahu and there are very few observations at this depth compared with higher up the profile.

380

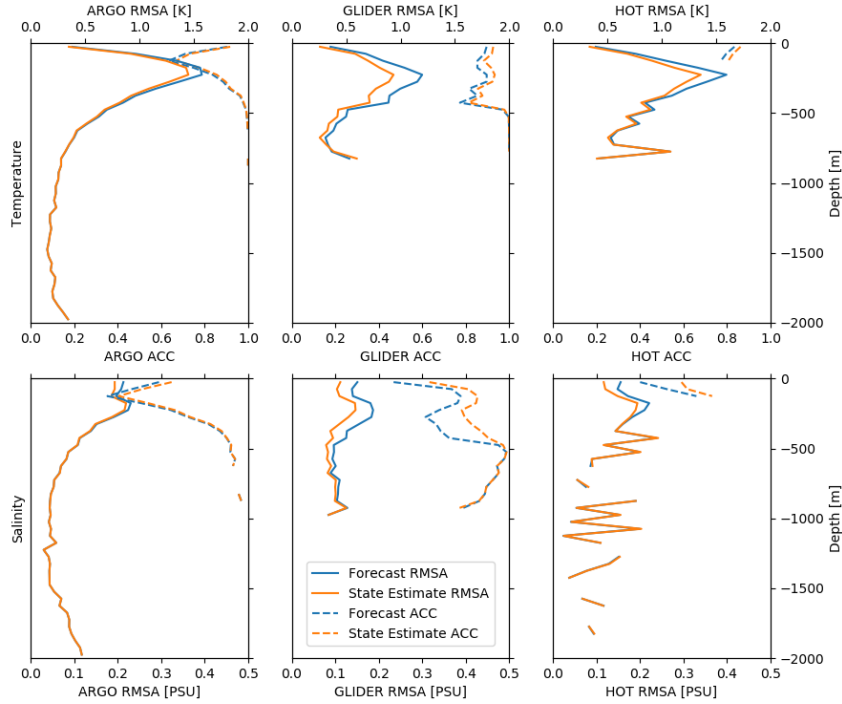
381

382

383

For subsurface salinity (fig. 11), the improvements made by the state-estimate solution occur almost exclusively about 500m for Argo floats and HOT CTDs. As with temperature

384



391 **Figure 11.** RMSA (solid) and ACC (dashed) profiles, binned by 50m intervals, of subsurface temperature  
 392 (top) and salinity (bottom) for Argo floats, SeaGliders and HOT CTDs.

385 the largest improvement is at the top of the thermocline. There are some low ACC values lower  
 386 down in the profile between both models and the observations, but both the forecast and state-  
 387 estimate perform equally at this depth. SeaGliders produce the biggest improvement in sub-  
 388 surface salinity model performance, with the state-estimate solution up to 20% better than the  
 389 forecast for both RMSA and ACC. The peak improvement is at the top of the thermocline,  
 390 but there are improvements throughout the profile.

### 393 5 Forecast Skill

In this section we quantify the model skill by using a skill score (SS), evaluated as the improvement against a reference field [Murphy, 1988]. For the reference, we use the persistence assumption and take the spatial location of each observation from the model field at the time of initialization for each cycle. The SS for the state estimate and forecast are defined as:

$$SS_a = 1 - \frac{\text{RMSA}(\mathbf{x}^a, \mathbf{y})}{\text{RMSA}(\mathbf{x}^0, \mathbf{y})}, \quad (6)$$

$$SS_f = 1 - \frac{\text{RMSA}(\mathbf{x}^f, \mathbf{y})}{\text{RMSA}(\mathbf{x}^0, \mathbf{y})}, \quad (7)$$

394 where the superscripts  $a$ ,  $f$ , and 0 refer to the state estimate, model forecast and persistence,  
 395 respectively. Under this measure, a SS of 1 represents a perfect fit between the model and ob-  
 396 servations, while a value of zero indicates where the model and persistence values perform ex-  
 397 actly the same. If the model is better than persistence, then the skill score will lie in the range  
 398  $0 < SS < 1$  and the degree of improvement over persistence is determined by how close  
 399 to 1 the score is. Conversely, a negative SS means the model is further from the observations  
 400 than persistence.

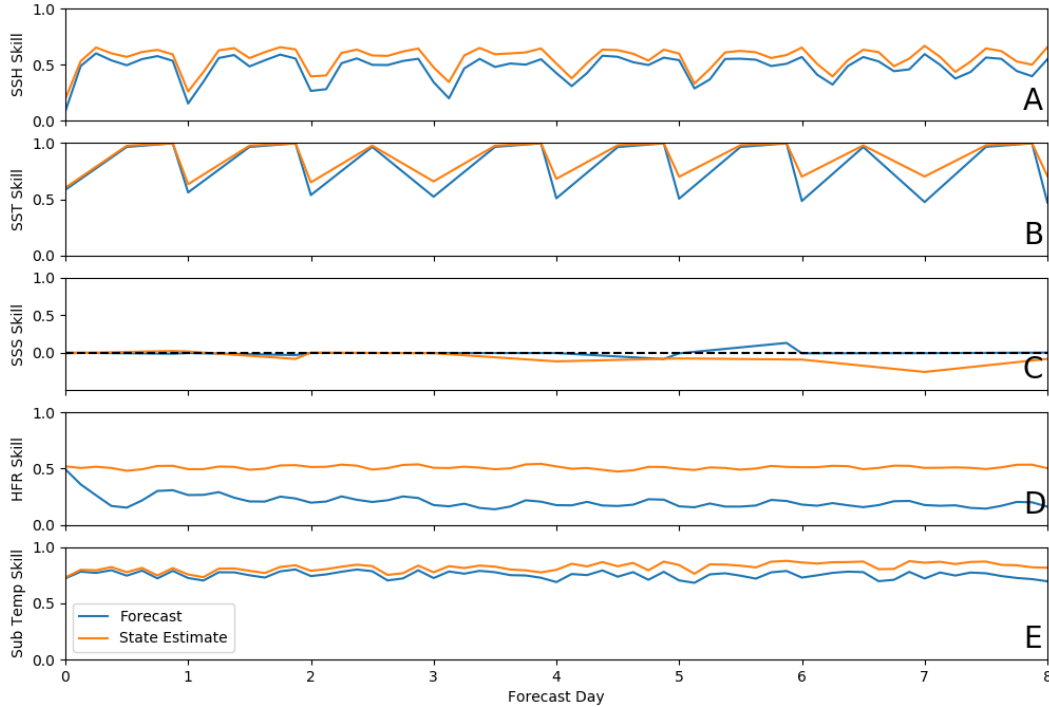
401 For this verification we wish to examine the effect of forecast length on the skill. Start-  
 402 ing with the same initial conditions as each state estimate cycle we produce an eight day fore-  
 403 cast, the length of two state estimate cycles. The RMSA is calculated every 3 hours for each  
 404 8-day forecast, the corresponding state-estimate cycles, and the persistence field from the start  
 405 of the forecast.

406 Figure 12 shows the mean SS over all cycles for remotely sensed observations. For SSH,  
 407 SST and HFR, the skill for both the state-estimation and free-running forecast is positive through-  
 408 out, indicating that both models are successful over persistence in representing those variables.  
 409 SSS however is close to zero and slightly negative meaning the models provide no better in-  
 410 formation than persistence. SST values are consistently the highest, with a reduction in skill  
 411 versus persistence for both models once per day. This is expected as the diurnal cycle means  
 412 the ocean temperature will be close to persistence once per day. For HFR the state-estimate  
 413 skill has a consistent value of 0.5 regardless of forecast day, while the forecast is closer to 0.2.

## 416 **6 Analysis of Increments**

417 During each I4D-Var 4-day window, the initial model field, as well as time-varying bound-  
 418 ary and surface forcings are adjusted to minimize the residuals. The initial condition incre-  
 419 ments form a single record for each cycle, while the boundary and surface forcings are per-  
 420 turbed every time they are applied to the model. The perturbations applied to the boundary  
 421 exhibit only a minor influence on the model (not shown), likely due to the sponge layer damp-  
 422 ening the signal. We focus our analysis on the increments of the initial conditions and the sur-  
 423 face forcing.

424 Over the 10 year reanalysis, there are 917 analysis cycles with sixteen surface forcing  
 425 adjustments (four per day) per cycle. We will examine the modes of variability of the incre-  
 426 ments via Empirical Orthogonal Functions (EOFs) [*Hannachi, 2004*].



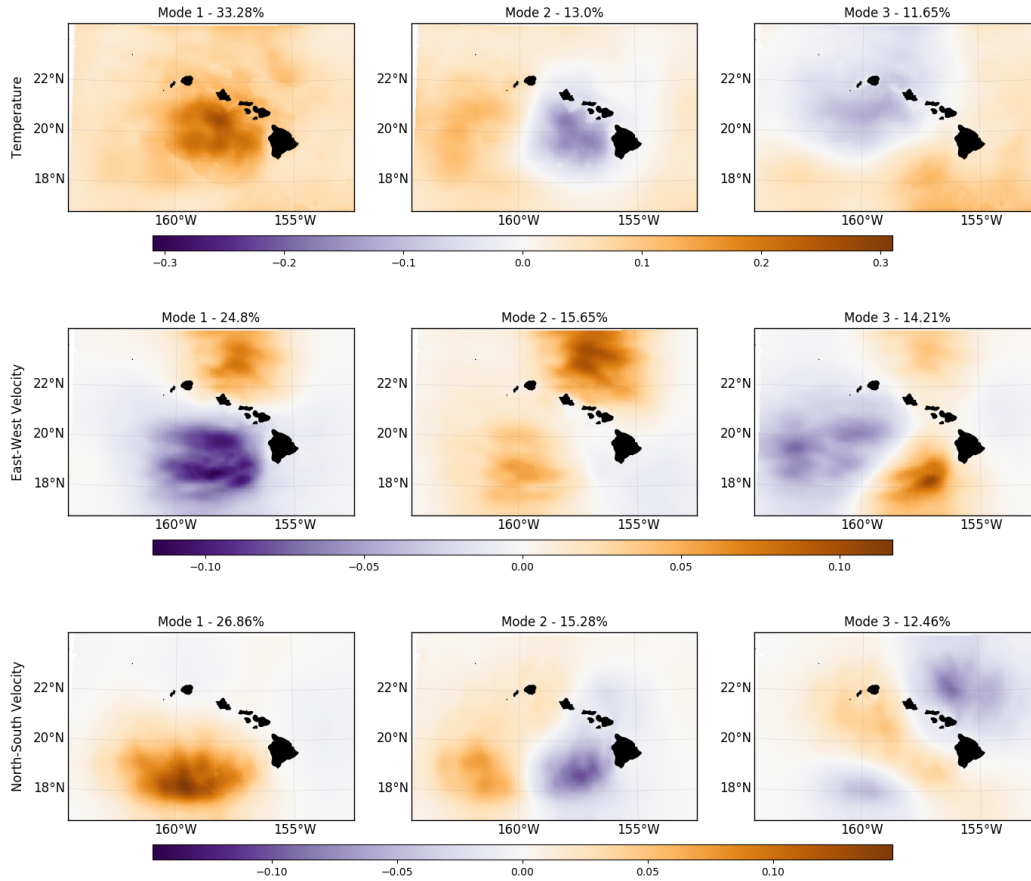
414 **Figure 12.** Mean skill metric for remotely sensed observations as a function of forecast length. A) Sea  
 415 Surface Height; B) Sea Surface Temperature; c) Sea Surface Salinity and D) HFRs

### 427 6.1 Initial Condition Perturbations

428 For each cycle, the initial perturbation of five main model variables are examined: sea  
 429 surface height, temperature, salinity, east-west velocity and north-south velocity. With the ex-  
 430 ception of sea surface height, each variable is averaged over the upper 100m to cover the mixed  
 431 layer. The increments for salinity and sea surface height as a percentage of the background  
 432 values are insignificant ( $< 1\%$ ), while temperature increments (2–10%) and the two veloc-  
 433 ity fields (10 – 20%) are significant enough to analyze.

434 Figure 13 shows the first three EOF modes for temperature and velocity increments to  
 435 the initial conditions. For temperature, the first mode accounts for 32% of the variance and  
 436 is positive across the entire domain with a peak in the region leeward of the islands, an area  
 437 known to have a strong temperature gradient [Xie *et al.*, 2001]. The second and third modes,  
 438 ( $\sim 11 - 13\%$  of variability) are also strongest in this region, albeit much weaker.

441 The first three modes of the velocity increments are closer in explained variance than  
 442 temperature, with the first accounting for  $\sim 25\%$  and the second and third  $\sim 15\%$ . The EOFs  
 443 exhibit a stronger signal further south than temperature, where the North Equatorial Current



439 **Figure 13.** EOF analysis of initial condition increments for upper 100m: top - temperature, middle - east-  
 440 west velocity and bottom - north-south velocity.

444 (NEC) flows past the islands and passes the Hawaiian Lee Counter Current (HLCC). Look-  
 445 ing at the east-west and north-south velocities in tandem, we can see that the dominant mode  
 446 is increasing the velocity to the north-west in this region. The secondary mode is weak in that  
 447 area for the east-west direction, with a split signal in the north south direction, while the third  
 448 mode shows the opposite. These modes are adjusting the state estimate for anti-cyclonic eddy  
 449 activity in lee of the Big Island.

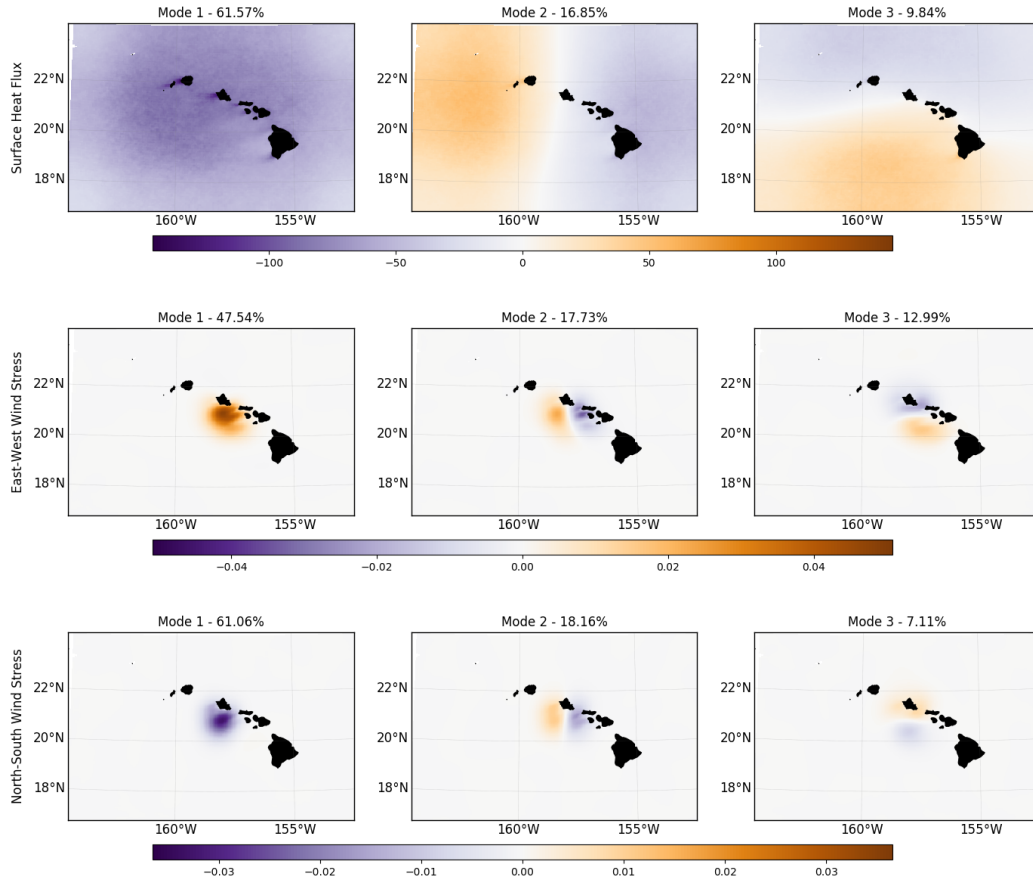
## 450 **6.2 Surface Forcing Perturbations**

451 The surface forcing increments are calculated every 6 hours during the assimilation and  
452 are linearly interpolated between this period. The time of day potentially impacts forcing vari-  
453 ables, particularly surface heat flux, so we calculate EOFs on the increments for each of the  
454 four distinct times of day they occur (00, 06, 12, 18 UTC). Due to the size of the model grid,  
455 the number of records and the computational resources available the EOF calculation is lim-  
456 ited to a 4-year period, approximately 1500 records. The results presented are the EOFs for  
457 the period 2007-2011; however other 4-year periods were also examined with no significant  
458 differences in the structure of the modes or their percentage variance explained. The time of  
459 day does impact the percentage variance explained by each mode, most notably for surface  
460 heat flux where the effect of diurnal solar heating occurs. The composition of the modes them-  
461 selves (i.e. where the peak/trough variances are located), have no significant difference for each  
462 time of day, so we present the average modes.

463 The four key surface forcing terms are: surface heat flux, surface salinity flux, east-west  
464 wind stress, and north-south wind stress. Of these, increments in surface salinity flux are small  
465 compared to their background value, while increments in surface heat flux (10–15% of back-  
466 ground) and the wind stresses (15–20%) are significant. The first mode dominates the ma-  
467 jority of the variability, particularly for surface heat flux where 60% is explained by this mode  
468 alone. For all three variables, the majority of the variability can be explained using the first  
469 5 modes.

470 The first three modes for the forcing terms are shown in Figure 14. For surface heat flux,  
471 we observe that the strongest mode, representing nearly 60% of the variability, is consistently  
472 negative over the region, essentially just accounting for the bias with the model. The strongest  
473 low in the region is leeward of the islands, similar to the first mode for the initial ocean tem-  
474 perature field and indicative that SST is being controlled by the surface heat flux. The sec-  
475 ond and third modes (16% and 10% of variance), split the domain vertically and horizontally,  
476 with a much weaker signal than the dominant mode. These two modes allow for large scale  
477 atmospheric gradients to contribute towards the surface heat forcing.

480 The EOFs of surface wind stress increments are confined to the shallow region close to  
481 the south coast of O’ahu, where the surface winds are likely to have the most impact on HFR.  
482 The strong singular signal from the dominant modes show a south-east high to adjust the winds;  
483 whereas, the secondary modes shows a diverging north-west to south-east split in the region  
484 account for more minor lee affects. The same signal does not appear in the initial condition



478 **Figure 14.** EOF analysis of atmospheric forcing perturbations; a) surface heat flux, b) east-west wind stress  
479 and c) north-south wind stress.

485 perturbations for velocity, likely because the wind stress has a significant effect on the surface  
486 flow.



## 487 **7 Summary**

488 We have presented a 10-year reanalysis of the PacIOOS Hawaiian Island Ocean Fore-  
489 cast System and assessed the performance of the state-estimate solution and free-running fore-  
490 casts. Using an updated model and data assimilation scheme, we show that the model repre-  
491 sents the observational data well over the time period. The largest improvement in the state-  
492 estimate solution occurs when minimizing the residuals to HFR data, with sea surface tem-  
493 perature also accounting for a significant improvement. On average, the assimilation achieves  
494 the near-optimal solution; however, the variability is heavily influenced by the HFR observa-  
495 tions. The analysis suggests the observational errors associated with HFR are too low and re-  
496 sults could be improved by redefining these errors. This is supported by the increase in vari-  
497 ability and upward trend of optimality towards the end of the time period where HFR obser-  
498 vations are most numerous.

499 The increments made by the reanalysis have revealed that sea surface height and salin-  
500 ity initial conditions aren't significantly adjusted by the I4D-Var procedure; whereas temper-  
501 ature and velocity account for a significant change from the forecast field. For the atmospheric  
502 forcing, surface salinity is insignificant, but the surface heat flux and wind stresses adjust the  
503 forcings by up to 20%. This corresponds to cost function statistics that show HFR and tem-  
504 perature as the two dominant observation sources. For each of these increments we performed  
505 an EOF analysis, where the first few modes explain most of the variability. Typically the first  
506 mode is dominant; In the atmospheric forcing increments the first mode is much more signif-  
507 icant than the others and tends to have a uniform direction indicating a bias adjustment. For  
508 surface heat flux this applies across the whole domain while wind stress increments are con-  
509 centrated in the region south of O'ahu. The wind stress heavily influences the surface currents  
510 and are mostly due to HFR. The secondary modes tended to show more oscillatory behavior  
511 to allow for atmospheric gradients and more minor effects.

512 The reanalysis has provided the testing for improvements to the PacIOOS operational  
513 forecast system. The data is being used to update the back catalog available publicly at [www.pacioos.org](http://www.pacioos.org)  
514 and will influence the future results from daily forecasts. Analysis of the I4D-Var increments  
515 has provided a greater understanding of the variability in the region and will provide the ba-  
516 sis for a move towards ensemble forecasting in the region.

## 517 **8 Code and Data Availability**

518 The ROMS code for running the model is available as an open source software pack-  
519 age distributed freely from <http://www.myroms.org>. The python code for working with the out-  
520 put is available from the repository [github.com/powellb/seapy](https://github.com/powellb/seapy).

521 Model initial conditions and boundary forcing comes from the HYbrid Coordinate Ocean  
522 Model ([hycom.org](http://hycom.org)). Atmospheric surface forcing and HFRadar observations are distributed  
523 through the PacIOOS data portal ([pacioos.hawaii.edu](http://pacioos.hawaii.edu)).

524 Satellite measurements come from two sources; sea surface temperature and salinity are  
525 provided by the Physical Oceanography Distributed Active Archive Centre ([podaac.jpl.nasa.gov](http://podaac.jpl.nasa.gov)),  
526 and surface height anomalies are provided by the Copernicus Marine Environment Monitor-  
527 ing Service ([marine.copernicus.eu](http://marine.copernicus.eu)).

528 In Situ measurements used are available from 3 sources; Argo measurements through  
529 Global Ocean Data Assimilation Experiment ([usgodae.org](http://usgodae.org)), SeaGliders through the School of  
530 Ocean and Earth Science and Technology at the University of Hawai'i at Manoa ([hahana.soest.hawaii.edu/seagliders](http://hahana.soest.hawaii.edu/seagliders)),  
531 and CTDs through the Hawaii Ocean Time-Series project ([hahana.soest.hawaii.edu/hot](http://hahana.soest.hawaii.edu/hot)).

532 Reanalysis output is produced as 3-hourly snapshots of the 3D fields temperature, salin-  
533 ity and velocities, as well as the 2D sea surface height field for the full time period. This data  
534 is archived through PacIOOS and can be made available for research purposes.

## 535 **Acknowledgements**

536 The authors would like to thank the GODAE for hosting the Argo observations and the  
537 HOT project for CTD and SeaGlider data. The authors would also like to thank Y.L. Chen of  
538 the University of Hawai'i Department of Meteorology for the atmospheric model data MM5  
539 and WRF.

## 540 **References**

- 541 Bennett, A. (2002), *Inverse Modeling of the Ocean and Atmosphere*, Cambridge University  
542 Press, doi:10.1017/CBO9780511535895.
- 543 Broquet, G., C. Edwards, A. Moore, B. Powell, M. Veneziani, and J. Doyle (2009), Ap-  
544 plication of 4d-variational data assimilation to the California current system, *Dynamics*  
545 *of Atmospheres and Oceans*, 48(1–3), 69 – 92, doi:10.1016/j.dynatmoce.2009.03.001,  
546 modeling and Data Assimilation in Support of Coastal Ocean Observing Systems.

- 547 Chapman, D. C. (1985), Numerical treatment of cross-shelf open boundaries in a  
548 barotropic coastal ocean model, *Journal of Physical Oceanography*, *15*(8), 1060–1075,  
549 doi:10.1175/1520-0485(1985)015<1060:NTOCSO>2.0.CO;2.
- 550 Chassignet, E. P., H. E. Hurlburt, O. M. Smedstad, G. R. Halliwell, P. J. Hogan, A. J.  
551 Wallcraft, R. Baraille, and R. Bleck (2007), The HYCOM (HYbrid Coordinate Ocean  
552 Model) data assimilative system, *Journal of Marine Systems*, *65*(1), 60 – 83, doi:  
553 10.1016/j.jmarsys.2005.09.016.
- 554 Chavanne, C., P. Flament, R. Lumpkin, B. Dousset, and A. Bentamy (2002), Scatterometer  
555 observations of wind variations induced by oceanic islands: Implications for wind-  
556 driven ocean circulation, *Canadian Journal of Remote Sensing*, *28*(3), 466–474, doi:  
557 10.5589/m02-047.
- 558 Courtier, P., J.-N. Thépaut, and A. Hollingsworth (1994), A strategy for operational im-  
559 plementation of 4d-var, using an incremental approach, *Quarterly Journal of the Royal*  
560 *Meteorological Society*, *120*(519), 1367–1387, doi:10.1002/qj.49712051912.
- 561 Egbert, G. D., A. F. Bennett, and M. G. G. Foreman (1994), Topex/poseidon tides esti-  
562 mated using a global inverse model, *Journal of Geophysical Research: Oceans*, *99*(C12),  
563 24,821–24,852, doi:10.1029/94JC01894.
- 564 Flather, R. (1976), A tidal model of the northwest european continental shelf, *Mem. Soc.*  
565 *R. Sci. Liege*, *10*(6), 141–164.
- 566 Hannachi, A. (2004), A primer for EOF analysis of climate data, *Tech. rep.*, Department of  
567 Meteorology, University of Reading.
- 568 HMRG (2017), Hawaii Mapping Research Group, SOEST. [http://www.soest.  
569 hawaii.edu/HMRG/multibeam/index.php](http://www.soest.hawaii.edu/HMRG/multibeam/index.php), Online, Last Checked 04/13/2018.
- 570 Janeković, I., and B. S. Powell (2012), Analysis of imposing tidal dynamics to nested  
571 numerical models, *Continental Shelf Research*, *34*, 30–40, doi:10.1016/j.csr.2011.11.017.
- 572 Janeković, I., B. S. Powell, D. Matthews, M. A. McManus, and J. Sevadjan (2013), 4d-  
573 var data assimilation in a nested, coastal ocean model: A Hawaiian case study, *Journal*  
574 *of Geophysical Research: Oceans*, *118*, 5022–5035, doi:10.1002/jgrc.20389.
- 575 Kerry, C., B. Powell, M. Roughan, and P. Oke (2016), Development and evaluation of a  
576 high-resolution reanalysis of the east australian current region using the regional ocean  
577 modelling system (ROMS 3.4) and incremental strong-constraint 4-dimensional varia-  
578 tional (is4d-var) data assimilation, *Geoscientific Model Development*, *9*(10), 3779–3801,  
579 doi:10.5194/gmd-9-3779-2016.

- 580 Lumpkin, R., and P. Flament (2013), Extent and energetics of the Hawaiian lee counter-  
581 current, *Oceanography*, 26(1), 58–65, doi:10.5670/oceanog.2013.05.
- 582 Matthews, D., B. S. Powell, and R. Milliff (2011), Dominant spatial variability scales  
583 from observations around the Hawaiian islands, *Deep-Sea Research*, 58(10), 979–987,  
584 doi:10.1016/j.dsr.2011.07.004.
- 585 Matthews, D., B. S. Powell, and I. Janeković (2012), Analysis of four-dimensional vari-  
586 ational state estimation of the Hawaiian waters, *Journal of Geophysical Research:*  
587 *Oceans*, 117, C03,013, doi:10.1029/2011JC007575.
- 588 Moore, A. M., H. G. Arango, E. D. Lorenzo, B. D. Cornuelle, A. J. Miller, and D. J.  
589 Neilson (2004), A comprehensive ocean prediction and analysis system based on the  
590 tangent linear and adjoint of a regional ocean model, *Ocean Modelling*, 7(1–2), 227 –  
591 258, doi:10.1016/j.ocemod.2003.11.001.
- 592 Moore, A. M., H. G. Arango, G. Broquet, B. S. Powell, A. T. Weaver, and J. Zavala-  
593 Garay (2011a), The Regional Ocean Modeling System (ROMS) 4-dimensional varia-  
594 tional data assimilation systems: Part I – system overview and formulation, *Progress in*  
595 *Oceanography*, 91(1), 34–49, doi:10.1016/j.pocean.2011.05.004.
- 596 Moore, A. M., H. G. Arango, G. Broquet, C. Edwards, M. Veneziani, B. Powell, D. Foley,  
597 J. D. Doyle, D. Costa, and P. Robinson (2011b), The Regional Ocean Modeling System  
598 (ROMS) 4-dimensional variational data assimilation systems: Part II – performance and  
599 application to the california current system, *Progress in Oceanography*, 91(1), 50 – 73,  
600 doi:10.1016/j.pocean.2011.05.003.
- 601 Moore, A. M., H. G. Arango, G. Broquet, C. Edwards, M. Veneziani, B. Powell, D. Fo-  
602 ley, J. D. Doyle, D. Costa, and P. Robinson (2011c), The Regional Ocean Modeling  
603 System (ROMS) 4-dimensional variational data assimilation systems: Part III – obser-  
604 vation impact and observation sensitivity in the california current system, *Progress in*  
605 *Oceanography*, 91(1), 74 – 94, doi:10.1016/j.pocean.2011.05.005.
- 606 Murphy, A. H. (1988), Skill scores based on the mean square error and their relation-  
607 ships to the correlation coefficient, *Monthly Weather Review*, 116(12), 2417–2424, doi:  
608 10.1175/1520-0493(1988)116<2417:SSBOTM>2.0.CO;2.
- 609 Oka, E., and K. Ando (2004), Stability of temperature and conductivity sensors of  
610 argo profiling floats, *Journal of Oceanography*, 60(2), 253–258, doi:10.1023/B:  
611 JOCE.0000038331.10108.79.

- 612 PacIOOS (2018), Pacific Islands Ocean Observing System. <http://www.pacioos.hawaii.edu/>, Online, Last Checked 04/13/2018.
- 613
- 614 Penenko, V. V. (2009), Variational methods of data assimilation and inverse problems for  
615 studying the atmosphere, ocean, and environment, *Numerical Analysis and Applications*,  
616 2(4), 341–351, doi:10.1134/S1995423909040065.
- 617 PO.DAAC (2005), UK Met Office. 2005. GHRSSST level 4 OSTIA global foundation sea  
618 surface temperature analysis. ver. 1.0.
- 619 PO.DAAC (2008), Naval Oceanographic Office. GHRSSST level 4 K10 global 1 meter sea  
620 surface temperature analysis. ver. 1.0.
- 621 PO.DAAC (2015), NASA Aquarius project. Aquarius official release level 3 sea surface  
622 salinity standard mapped image daily data v4.0.
- 623 Powell, B., H. Arango, A. Moore, E. D. Lorenzo, R. Milliff, and D. Foley (2008), 4DVAR  
624 data assimilation in the Intra-Americas sea with the Regional Ocean Modeling System  
625 (ROMS), *Ocean Modelling*, 25(3–4), 173 – 188, doi:10.1016/j.ocemod.2008.08.002.
- 626 Sasaki, H., and P. Klein (2012), Ssh wavenumber spectra in the north pacific from a high-  
627 resolution realistic simulation, *Journal of Physical Oceanography*, 42(7), 1233–1241,  
628 doi:10.1175/JPO-D-11-0180.1.
- 629 Shchepetkin, A. F., and J. C. McWilliams (1998), Quasi-monotone advection schemes  
630 based on explicit locally adaptive dissipation, *Monthly Weather Review*, 126(6), 1541–  
631 1580, doi:10.1175/1520-0493(1998)126<1541:QMASBO>2.0.CO;2.
- 632 Shchepetkin, A. F., and J. C. McWilliams (2003), A method for computing horizontal  
633 pressure-gradient force in an oceanic model with a nonaligned vertical coordinate,  
634 *Journal of Geophysical Research: Oceans*, 108(C3), doi:10.1029/2001JC001047, 3090.
- 635 Shchepetkin, A. F., and J. C. McWilliams (2005), The Regional Oceanic Modeling System  
636 (ROMS): A split-explicit, free-surface, topography-following-coordinate oceanic model,  
637 *Ocean Modelling*, 9(4), 347–404, doi:10.1016/j.ocemod.2004.08.002.
- 638 Simmons, A. J., J. M. Wallace, and G. W. Branstator (1983), Barotropic wave propagation  
639 and instability, and atmospheric teleconnection patterns, *Journal of the Atmospheric  
640 Sciences*, 40(6), 1363–1392, doi:10.1175/1520-0469(1983)040<1363:BWPAIA>2.0.CO;2.
- 641 Smith, R. B., and V. Grubišić (1993), Aerial observations of Hawaii’s wake, *Journal of  
642 the Atmospheric Sciences*, 50(22), 3728–3750, doi:10.1175/1520-0469(1993)050<3728:  
643 AOOHW>2.0.CO;2.

- 644 Souza, J. M. A. C., B. S. Powell, A. C. Castillo-Trujillo, and P. Flament (2015), The  
645 vorticity balance of the ocean surface in Hawaii from a regional reanalysis, *Journal of*  
646 *Physical Oceanography*, 45(2), 424–440, doi:10.1175/JPO-D-14-0074.1.
- 647 Stammer, D., C. Wunsch, R. Giering, C. Eckert, P. Heimbach, J. Marotzke, A. Adcroft,  
648 C. N. Hill, and J. Marshall (2002), Global ocean circulation during 1992–1997, esti-  
649 mated from ocean observations and a general circulation model, *Journal of Geophysical*  
650 *Research: Oceans*, 107(C9), 1–1–1–27, doi:10.1029/2001JC000888, 3118.
- 651 Talagrand, O., and P. Courtier (1987), Variational assimilation of meteorological obser-  
652 vations with the adjoint vorticity equation. I: Theory, *Quarterly Journal of the Royal*  
653 *Meteorological Society*, 113(478), 1311–1328, doi:10.1002/qj.49711347812.
- 654 USGODAE (2016), Argo floats data from global data assembly centre  
655 doi:10.17882/42182.
- 656 Weaver, A. T., J. Vialard, and D. L. T. Anderson (2003), Three- and four-dimensional  
657 variational assimilation with a general circulation model of the tropical pacific ocean.  
658 part i: Formulation, internal diagnostics, and consistency checks, *Monthly Weather*  
659 *Review*, 131(7), 1360–1378, doi:10.1175/1520-0493(2003)131<1360:TAFVAW>2.0.CO;2.
- 660 WRF-ARW (2017), Hawaii Weather Research and Forecasting, SOEST. [http://www.](http://www.soest.hawaii.edu/MET/Faculty/wrf/arw/arw_state_6km.html)  
661 [soest.hawaii.edu/MET/Faculty/wrf/arw/arw\\_state\\_6km.html](http://www.soest.hawaii.edu/MET/Faculty/wrf/arw/arw_state_6km.html), On-  
662 line, Last Checked 04/13/2018.
- 663 Xie, S. P., W. T. Liu, Q. Y. Liu, and M. Nonaka (2001), Far-reaching effects of the  
664 Hawaiian islands on the pacific ocean-atmosphere system, *Science*, 292(5524), 2057–  
665 2060, doi:10.1126/science.1059781.
- 666 Yang, Y., Y.-L. Chen, and F. M. Fujioka (2008a), Effects of trade-wind strength and di-  
667 rection on the leeside circulations and rainfall of the island of Hawaii, *Monthly Weather*  
668 *Review*, 136(12), 4799–4818, doi:10.1175/2008MWR2365.1.
- 669 Yang, Y., S.-P. Xie, and J. Hafner (2008b), Cloud patterns lee of Hawaii island: A synthe-  
670 sis of satellite observations and numerical simulation, *Journal of Geophysical Research*,  
671 113(D15), doi:10.1029/2008JD009889.
- 672 Zanife, O. Z., P. Vincent, L. Amarouche, J. P. Dumont, P. Thibaut, and S. Labroue (2003),  
673 Comparison of the Ku-band range noise level and the relative sea-state bias of the  
674 Jason-1, TOPEX, and Poseidon-1 radar altimeters, *Marine Geodesy*, 26(3-4), 201–238,  
675 doi:10.1080/714044519.

676 Zhang, W. G., J. L. Wilkin, and H. G. Arango (2010), Towards an integrated ob-  
677 servation and modeling system in the New York bight using variational meth-  
678 ods. Part I: 4DVAR data assimilation, *Ocean Modelling*, 35(3), 119 – 133, doi:  
679 10.1016/j.ocemod.2010.08.003.